Identification of a spatially distributed diffusion model for simulation of temporal cellular growth

Hanna Piotrzkowska-Wróblewska [a], Jacek M. Bajkowski [b] [iD],*, Bartłomiej Dyniewicz [a], Czesław I. Bajer [a]

[a] *Institute of Fundamental Technological Research, Polish Academy of Sciences, Pawinskiego 5b, Warsaw, 02-106, Poland*
[b] *Faculty of Mechanical and Industrial Engineering, Warsaw University of Technology, Narbutta 85, Warsaw, 02-524, Poland*

ARTICLE INFO

ABSTRACT

This study introduces a spatially distributed diffusion model based on a Navier–Stokes formulation with a pseudo-velocity field, providing a framework for modelling cellular growth dynamics within diseased tissues. Five coupled partial differential equations describe diseased cell development within a two-dimensional spatial domain over time. A pseudo-velocity field mimics biomarker concentration increasing over time and space, influencing tumour growth dynamics. An S-shape coupling functions for individual equations were assumed to establish the mathematical relationship between parameters and variables. The parameters were identified in a minimisation procedure to validate the model's efficacy based on limited clinical data. While the model draws inspiration from applications in oncology and could potentially be adopted for treatment planning and evaluation, it can also be helpful in applications from developmental biology to tissue engineering in clinical and experimental settings.

1. Introduction

Models of cancer development often focus on describing temporal dynamics at a single spatial point where certain variables, like the tumour size, are specified. They typically employ ordinary differential equations (ODEs) or second-order parabolic partial differential equations (PDEs). The primary objective of ODE-based models involves selecting the initial conditions and time-varying coefficients. These models require a small number of parameters, which are relatively straightforward to adjust and often provide explicit time-based solutions. While these models illustrate cell growth through saturating functions, they fail to account for the spatial distribution of cells and processes such as blood vessel evolution, spatial heterogeneity and others observed in clinical settings. The proposed model extends these approaches by incorporating spatial distribution and dynamic interactions specific to cancer progression.

Under certain assumptions, living tissues, including tumours, can be modelled using fluid dynamics (Chaplain, 1996). Consequently, some models use Navier–Stokes equations or their generalisations, such as Darcy's law, Stokes' law, or Brinkman's law, to govern cell development dynamics (Lowengrub et al., 2010; Donatelli and Trivisa, 2015; Cai et al., 2016; Lefebvre et al., 2016). Cristini et al. used a coupled system of PDEs to simulate tumour growth and angiogenesis, treating the tumour as an incompressible fluid with velocity governed by Darcy's law, accounting for fluid flow and pressure-driven cell movement (Cristini et al., 2003). Hubbard and Byrne incorporated mass and momentum conservation for tumour cells, blood vessels, and extracellular material, including diffusible nutrients (Hubbard and Byrne, 2013). Koomullil et al. employed Navier–Stokes equations and diffusion models for transport processes (Koomullil et al., 2021), while Bresch et al. combined three-dimensional Navier–Stokes equations with spatial diffusion models to illustrate the cell cycle progression conditioned by the tumour microenvironment (Bresch et al., 2010). Further refinements incorporated bidirectional control processes, where tumour cells and blood vessels mutually influence each other (Hahnfeldt et al., 1999). Watanabe et al. (2016) proposed a simpler mathematical model with three first-order ODEs, capturing growth saturation.

Building on these concepts, the model presented in this paper incorporates spatial and temporal dependencies related to tissue growth, vascular development, and Ki-67 marker levels. It employs a Navier–Stokes formulation with a pseudo-velocity field, using momentum equations for protein propagation and additional equations for diffusive processes. Coupling functions connect these processes, and their parameters and shape coefficients are determined through minimisation against available data. Such parameter identification enables
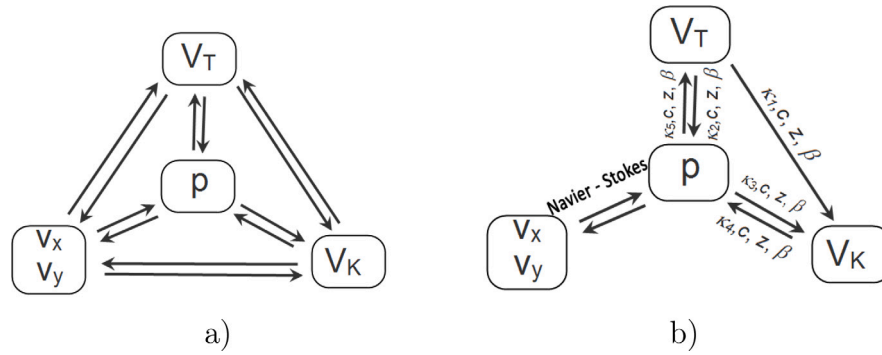

Fig. 1. Full set of relations among system variables –(a) and the reduced variant –(b).

simulating disease progression and improving therapy selection. By aligning the model with broader clinical observations, the authors aim to improve its ability to predict treatment outcomes for diverse clinical cases.

2. Methods

2.1. Mathematical model

Analysis of cell development reveals growth characteristics similar to physical processes where mass diffuses from higher to lower potential regions. Therefore, fluid flow, propagation, and diffusion models can effectively map relationships in disease-affected tissues. Consequently, in our paper, tumour growth is modelled as a diffusion process coupled with a modified Navier–Stokes equation for an incompressible fluid and a pseudo-velocity field.

A two-dimensional model is introduced. The model considers four variables emulating interactions influencing the cell growth dynamics and an apparent velocity field vector, namely:

1. $V_T(x, y, t)$ — tumour concentration representing the percentage of diseased cells in a unit volume of tissue at time t,
2. $V_K(x, y, t)$ — vascularised tissue concentration, representing the percentage of tissue volume occupied by blood vessels,
3. $p(x, y, t)$ — protein Ki-67 concentration, serving as a marker for tumour development,
4. $\mathbf{v}(x, y, t) = \{v_x, v_y\}^{\mathrm{T}}$ — apparent velocity field vector for protein propagation.

Although the model could be extended into three dimensions, this would significantly increase the computational effort. The relationships among variables influencing cell growth dynamics suggest mutual interactions, represented by arrows in Fig. 1a. These can be described using coupling functions with specific shape parameters like κ, c, z, β, described later.

Variables in the model can be linked implicitly, through coefficient functions in the derivatives, or explicitly by shifting terms to the right-hand side. Mixed couplings are also possible. In practice, these methods produce similar results, although starting with explicit couplings simplifies early development and testing. By focusing on the Ki-67 protein concentration (p), the complex system (Fig. 1a) was reduced to a simpler form with fewer interconnections (Fig. 1b), easing computational effort during minimisation.

A growing tumour increases the number and size of vessels formed through vasculogenesis and angiogenesis ($V_T \rightarrow V_K$), allowing blood vessels to penetrate from primary locations into areas of high tumour cell concentration. The fraction of actively dividing cancer cells, indicated by the presence of the Ki-67 protein, correlates with enhanced infiltration into surrounding tissues. Proliferation depends on vascularisation, as blood vessels supply nutrients and oxygen while removing waste ($V_T \leftrightarrow p$, $V_k \leftrightarrow p$). Tumour expansion, driven by proliferating

and infiltrating cells, spreads as a diffuse front ($v_x, v_y^{\mathrm{T}} \leftrightarrow p$) around the tumour core and vessel formation zones.

The dynamics of cell development can be thus coupled as a set of the following differential equations:

$$
\begin{cases}
\alpha_T \left(\frac{\partial^2 V_T}{\partial x^2} + \frac{\partial^2 V_T}{\partial y^2} \right) = \frac{\partial V_T}{\partial t} - \tilde{f}_T(x, y, V_K, p) & \text{(a)} \\
\alpha_K \left(\frac{\partial^2 V_K}{\partial x^2} + \frac{\partial^2 V_K}{\partial y^2} \right) = \frac{\partial V_K}{\partial t} - \tilde{f}_K(x, y, V_T, p) & \text{(b)} \\
\rho \frac{\partial v_x}{\partial t} + \rho \left(v_x \frac{\partial v_x}{\partial x} + v_y \frac{\partial v_x}{\partial y} \right) - \mu \left(\frac{\partial^2 v_x}{\partial x^2} + \frac{\partial^2 v_x}{\partial y^2} \right) + \frac{\partial p}{\partial x} = \tilde{f}_{px}(x, y, V_T, V_K) & \text{(c)} \\
\rho \frac{\partial v_y}{\partial t} + \rho \left(v_x \frac{\partial v_y}{\partial x} + v_y \frac{\partial v_y}{\partial y} \right) - \mu \left(\frac{\partial^2 v_y}{\partial x^2} + \frac{\partial^2 v_y}{\partial y^2} \right) + \frac{\partial p}{\partial y} = \tilde{f}_{py}(x, y, V_T, V_K) & \text{(d)} \\
\frac{\partial v_x}{\partial x} + \frac{\partial v_y}{\partial y} = 0 & \text{(e)}
\end{cases}
$$

$$(1)$$

The first two equations ((1a), (1b)) govern the diffusion of proliferating cells and vascular tissue, with α_T and α_K as their respective diffusion coefficients. The following three equations ((1c), (1d), (1e)) are modified Navier–Stokes equations. The momentum equations ((1c), (1d)) describe the evolution of the velocity components v_x and v_y, with μ as the apparent viscosity influencing flow propagation and ρ as the apparent inertia opposing the spread of Ki-67-producing cells. The continuity Eq. (1e) enforces incompressibility, ensuring that the variables are coupled and cannot increase independently in both directions.

A square region Ω of 40 mm edge was considered, with boundary conditions equal to 0 for all variables at the edge $\partial\Omega$

$$\forall_{t \geq 0}(V_T, V_K, v_x, v_y, p) = 0 \quad \text{on} \quad \partial\Omega.$$

The initial conditions were as follows

$$\forall_{(x,y) \in \Omega, t=0}(V_T, V_K, v_x, v_y, p) = 0 .$$

Functions $\tilde{f}$ introduce interdependence among unknowns, linking each equation's solution to the others. Each $\tilde{f}$ can be expressed as a sum of S-type functions which capture initial slow growth, rapid increase, and eventual saturation, described by

$$f(\chi, \kappa, c, z, \beta) = \kappa \left(e^{-\frac{1}{c} \exp(-\beta c \chi / z)} - e^{-1/c} \right) (1 - e^{-1/c})^{-1} , \qquad (2)$$

where χ is the primary variable, κ scales the saturation, c sets steepness and compression, z determines the input range for near-maximal values, and β influences the rate of change within the exponential function. Examples of these function shapes are provided in the Supplementary Material.

In Fig. 1a, each arrow indicating coupling via the S-function could have its own parameters κ, β, c, and z, requiring to minimise at least 48 coupling parameters. The reduced model presented in Fig. 1b requires a maximum of 20 coupling function parameters and separate coefficients for the Navier–Stokes equation. To further balance the computational feasibility, it was assumed that the S-function shape for all couplings remains the same (i.e. β, c and z are the same), differing only in scaling factor value κ.
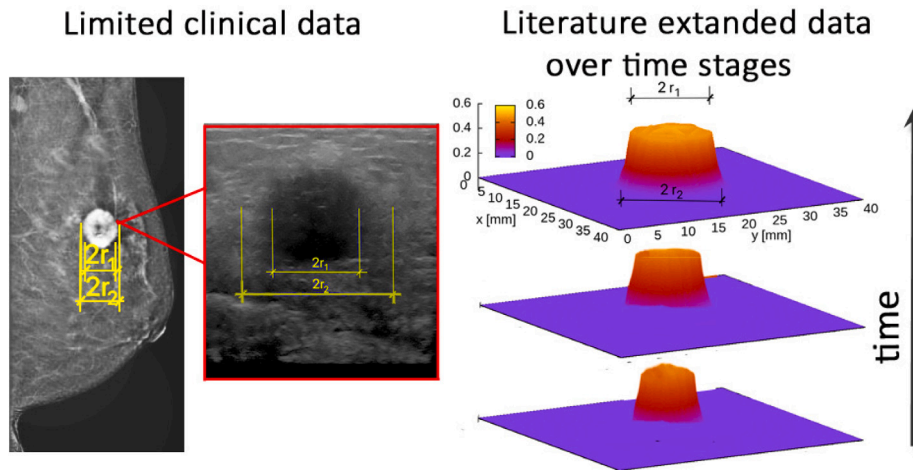
Fig. 2. Malignant tumour image and corresponding trapezoidal tumour shape defined by radii r_1 and r_2.

2.2. Solution

The system of equations was solved numerically using the finite element method on a mesh of 3200 triangular elements. Due to non-linear dependencies, a linear approximation of the variables was employed. Although a second-order Runge–Kutta method was used for time integration, an Euler method would yield similar accuracy.

Fig. 2 shows an ultrasound image of a malignant tumour in a 47-year-old female patient, obtained from the Radiology Department at Maria Sklodowska-Curie National Research Institute of Oncology, Warsaw, Poland. Written consent was provided, and the single-centre study adhered to the Declaration of Helsinki and was approved by the MSCNRIO Ethics Committee.

An indistinct tumour boundary was assumed, transitioning from a smaller radius r_1 (fully occupied by malignant cells) to a larger radius r_2 (marking the beginning of healthy tissue). As r_1, r_2, and trapezoid heights change over time, the reference function forms a trapezoidal shape (Fig. 2) representing tumour cell saturation. According to Mao et al. (2019), Weedon-Fekjaer et al. (2008), tumour volume doubles in about 280 days, while its linear dimension doubles in approximately 440 days. A series of trapezoidal profiles was thus created to illustrate the tumour's development over time.

The model comprises five unknowns and multiple parameters, initially treated as unknowns during error minimisation to align with clinical data. Once identified, these parameters remain fixed in the governing equations. Parameter selection and functional minimisation involve iteratively modifying randomly chosen variables within a range of zero to one (see Appendix for details). Some variables remain unchanged, while others adopt values from the current best solution, allowing exploration of neighbourhoods around it. Adjusting the number of altered variables shifts the approach between a Monte Carlo-like search and a method resembling gradient-based optimisation.

The system defined by Eqs. (1a)–(1d) requires four parameters: α_T, α_K, ρ, and μ. The reduced interaction model (Fig. 1b) introduces eight more: c, z, β, and κ_1 to κ_5. A threshold value T_v for the relation $p \rightarrow V_T$ was also introduced. In total, thirteen parameters must be identified:

- **1–4**: α_T, α_K, ρ and μ, being parameters of Eqs. (1a)–(1d),
- **5–9**: being scaling factors κ of the coupling functions $\tilde{f}$, in particular κ_1 for influencing $V_T \rightarrow V_K$, κ_2 for $V_T \rightarrow p$, κ_3 for $p \rightarrow V_K$, κ_4 for $V_K \rightarrow p$, and κ_5 for $p \rightarrow V_T$,
- **10–12**: c, z and β, being shape coefficients of the S-functions (Eq. (2)), assumed identical for all shape functions,

- **13**: T_v being a threshold for the relation $p \rightarrow V_T$, which sets the maximum value for the concentration of cancer cells in the tissue; this value is based on clinical data, specific for the type of tumour and the degree of cell calcification.

Solving the initial boundary value problem with a grid of 1681 nodes and 3362 unknowns for a single dataset takes about eight minutes on a single thread of an Xeon W-2145 3.7 GHz processor. Given this lengthy process, optimisation with many decision variables is very time-consuming. Therefore, it is logical to separate variables with minor impacts on the objective function from those with significant impacts.

The objective functional I, defined as the $\| \cdot \|_2$ norm, represents the difference between the assumed tumour profile V_T^* given at N grid points (x_i, y_i) located in the observed region, with i indexing the grid points, over four successive stages of evolution at time t_k, and the profile obtained through simulation with fixed decision variables. In our case, points located along the diameter of the tumour were assumed for observation:

$$I = \sqrt{\sum_{k=1}^{4} \sum_{i=1}^{N} \left[V_T^*(x_i, y_i, t_k) - V_T(x_i, y_i, t_k) \right]^2} \,. \tag{3}$$

The error metric (3) can be extended to include additional model variables by adding terms to the sums and assigning appropriate weights when clinical data are available.

3. Results

Due to the non-convex nature of the functional, multiple local optima may occur, producing similar objective values at different points in the feasible solution space. The top-left plot in Fig. 3 shows bar-plotted error values for suboptimal cases, while exact error values appear in the Supplementary Material Table.

Although the top four solutions differ by less than 6% in error value, their parameter sets vary considerably. Thus, these results should be viewed as illustrative, reflecting the specific literature data. The inverse problem solutions are suboptimal and may represent widely differing variable sets. Future improvements require gathering more clinical data to improve the accuracy and predictive capabilities of the simulations, ultimately assisting in personalised treatment planning and outcome assessment. Nevertheless, including additional medical and model-related parameters increases computational costs and complicates alignment with clinical data. To address these challenges, several improvements

can be recommended. First, replacing the traditional time-stepping with a space–time finite element formulation using simplex-shaped bases reduces computational costs proportionally to the number of unknowns. Second, leveraging GPUs (Dyniewicz et al., 2023) enables processing each time step as a sequence of matrix–vector operations, maintaining efficiency as the number of unknowns grows. Finally, introducing hybrid random-gradient methods for error minimisation further decreases the computational burden when fitting the model to clinical data.

Fig. 3 presents optimised model parameters as bar plots. The bars on the left represent the most accurate solutions, which are more reliable for analysis. Parameters with bars of similar height indicate high sensitivity of solution, as small changes in their values significantly affect the system's behaviour, requiring precise determination. In contrast, parameters with varied bar heights influence the solution less, allowing similar results with differing values. These can be initially estimated with lower accuracy since further refinement offers limited improvement.

For example, the wide variability of variable 4 suggests minimal impact on the final solution, allowing similar results over a broad range of its values. In contrast, the consistent patterns of variables 5 and 8, even among suboptimal solutions, highlight their critical influence and prevent arbitrary selection of their values. Suboptimal cases with lower fitting errors represent more accurate solutions, warranting closer examination during analysis.

Thus, variables 1, 3, 5, and 7–11 strongly influence the solution, while variables 2, 4, 6, 12, and 13 have minimal impact on the objective function. In particular, variables 4, 6, and 13 can vary widely, even reaching permissible extremes, without significantly altering the objective function.

Fig. 4 shows the tumour's simulated spatial progression, beginning with a single central lesion. A second lesion was introduced, eventually fusing with the first, forming a transitional zone. As saturation increases and then declines along a trapezoidal pattern (Fig. 2), the model reflects multifocal breast cancer dynamics, observed in 6%–60% of cases (Masannat et al., 2019). When tumours exceed 5 cm, separate foci often merge into a single mass. This modelling approach can simulate disease progression and predict tumour regression rates under neoadjuvant therapies, where fragmentation into multiple foci often indicates a positive treatment response.

Fig. 5 demonstrates close agreement between simulated trapezoidal shapes and those derived from clinical and literature data. Fig. 6 presents the apparent diffusion rate of dividing cells $|\mathbf{v}|$, showing zero velocity where tumour regions converge due to similar concentrations, and thus no net flow. Incorporating tissue necrosis into the model is possible, but additional clinical data is required.

Fig. 7 shows the spatial distribution of Ki-67 protein production, which remains limited to initial tumour sites, spreading slowly. This indicates that early intervention can be more effective, as the protein source region remains localised even when the tumour has grown substantially.

The model's feasibility was evaluated using two scenarios. First, reference data from Lundgren (1977), providing initial and observed tumour sizes and doubling times, were used to validate one selected case (Fig. 8, Case 1). A second scenario introduced a slower initial growth phase followed by a rapid increase (Fig. 8, Case 2) to test the model's ability to capture altered dynamics.

Fig. 9 compares four successive cross-sectional profiles from the reference case with simulated results, showing close alignment for both Case 1 (Fig. 9a) and Case 2 (Fig. 9b).

Fig. 10 presents smoothed temporal distributions of cancer cell concentrations, indicating that although Case 2's growth pattern differs, both scenarios ultimately converge to the same distribution after 20 months. This confirms the model's capability to represent various growth trajectories.
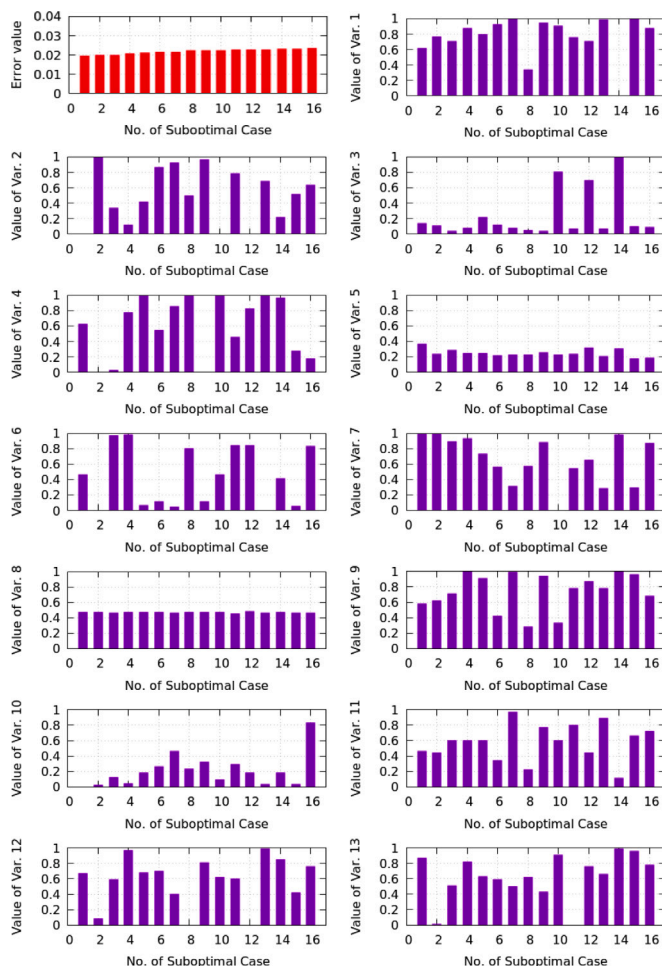

Fig. 3. Error values for sub-optimal solutions (top-left) and corresponding normalised values of variables 1–13.

4. Conclusions

This study introduced a novel spatially distributed diffusion model for simulating temporal cellular growth, implemented using a custom finite element-based program combined with minimisation techniques. A notable strength of the model is its low sensitivity to specific parameters, allowing these to be fixed as constants and thereby simplifying the computations. This reduction effectively constrains the solution space to those consistent with clinical data, enabling the acceptance of sub-optimal solutions as final outcomes within the model's framework.

The model successfully identifies significant factors influencing treatment effectiveness, enhancing its potential to predict patient conditions at various disease stages. Future enhancements will extend the model to include treatment and post-treatment phases, integrating patient-specific parameters and therapy characteristics.

Despite its promising capabilities, the current study is limited by a small sample size. Addressing this limitation will involve collecting a larger and more diverse set of clinical data and refining the parameter selection process. Ongoing research will focus on optimising the number and types of parameters to improve the model's accuracy and reliability, strengthening its utility in clinical decision-making and personalised treatment planning.
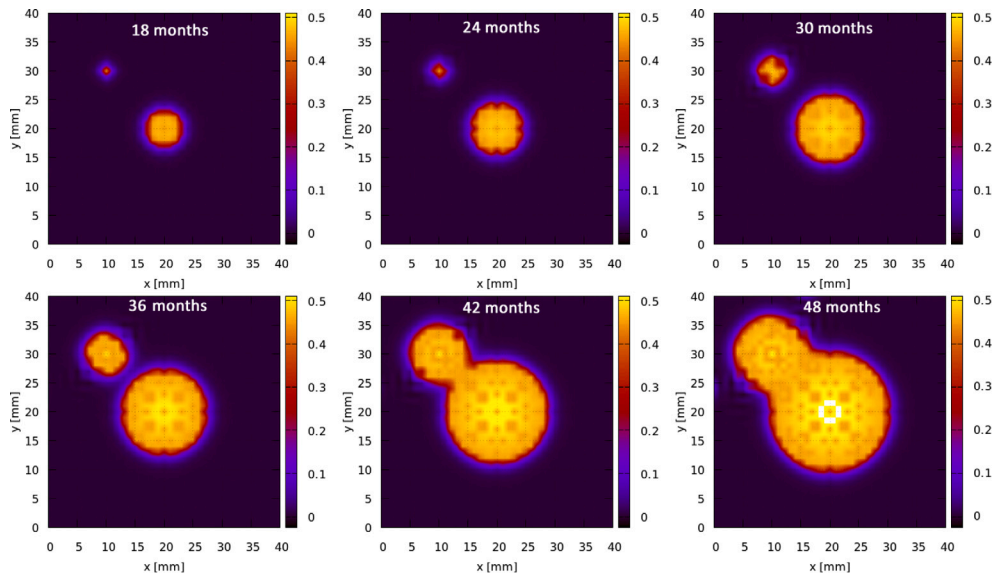
Fig. 4. Successive stages of tumour concentration V_T with metastasis evolution at 18, 24, 30, 36, 42, and 48 months.
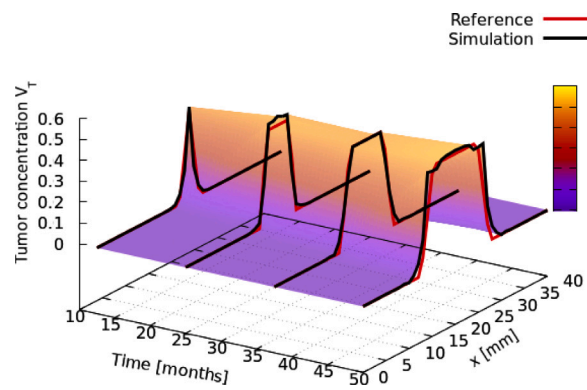

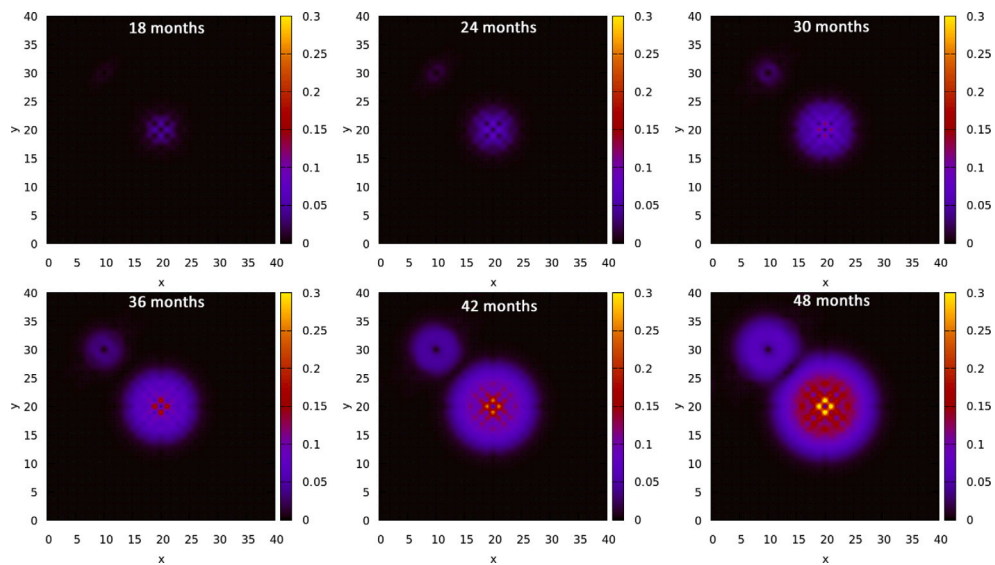**Fig. 5.** Comparison of tumour profile shapes from simulation and reference clinical data.

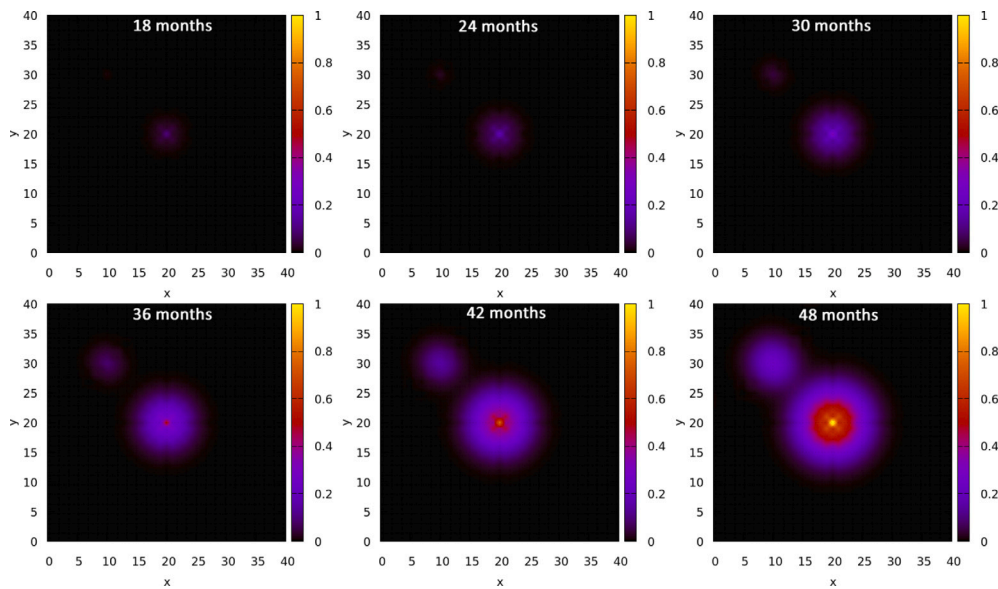**Fig. 6.** Successive velocity stages $|\mathbf{v}|$ distribution after 18, 24, 30, 36, 42, and 48 months.

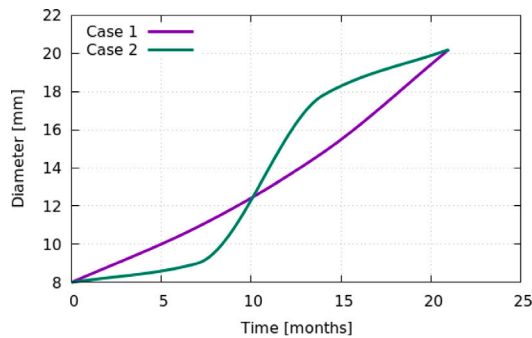**Fig. 7.** Successive stages of protein concentration *p* at 18, 24, 30, 36, 42, and 48 months.

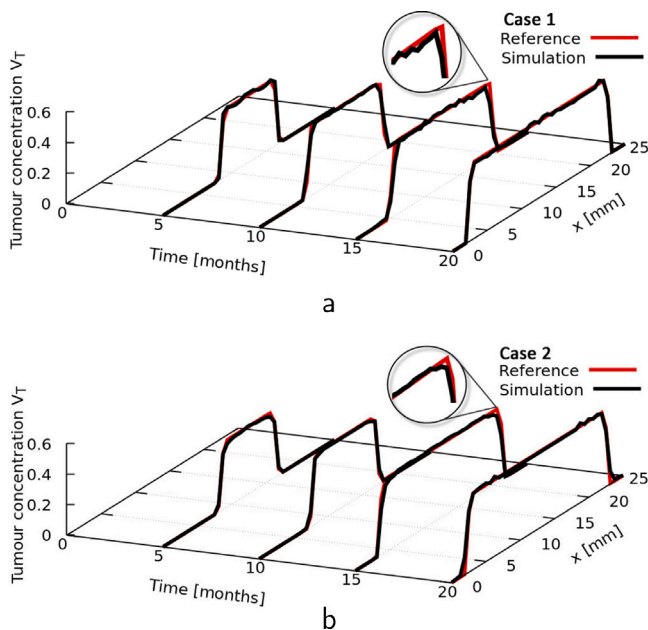**Fig. 8.** Two cases of tumour evolution, based on literature (Case 1) and an arbitrary curve (Case 2).

Fig. 9. Comparison of tumour profile growth dynamics for Case 1 –(a) and Case 2 –(b).

CRediT authorship contribution statement

Hanna Piotrzkowska-Wróblewska: Writing – original draft, Resources, Funding acquisition, Data curation. **Jacek M. Bajkowski:** Writing – review & editing, Writing – original draft, Investigation, Formal analysis. **Bartłomiej Dyniewicz:** Writing – original draft, Software, Funding acquisition. **Czesław I. Bajer:** Writing – original draft, Visualization, Software, Methodology, Investigation, Formal analysis, Data curation.

Declaration of competing interest

The authors declare the following financial interests/personal relationships which may be considered as potential competing interests: Hanna Piotrzkowska-Wroblewska reports financial support was provided by National Centre for Research and Development. Bartlomiej Dyniewicz reports financial support was provided by National Science Centre Poland. Czeslaw Bajer reports financial support was provided by National Science Centre Poland. If there are other authors, they declare that they have no known competing financial interests or personal relationships that could have appeared to influence the work reported in this paper.

Acknowledgements

Appendix A. Supplementary data

Supplementary material related to this article can be found online at https://doi.org/10.1016/j.jbiomech.2025.112581.

Data availability

The coding sequence and scripts are available to download from the authors website (http://bluebox.ippt.pan.pl/~{}cbajer/), while custom numerical tools and data for replication are available upon request from the corresponding author J. M. Bajkowski.
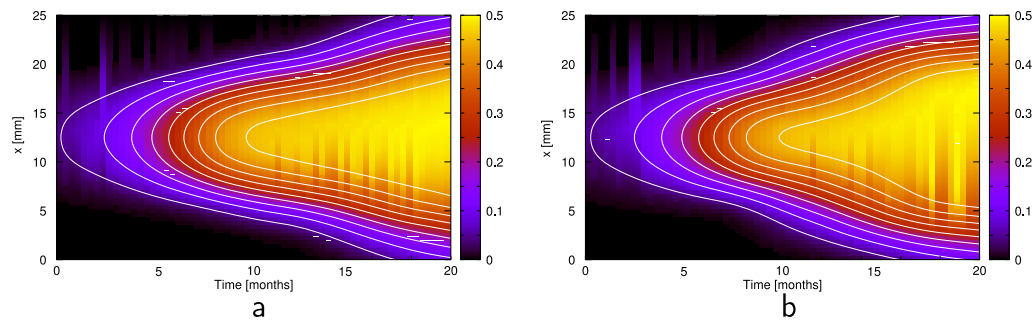
Fig. 10. Temporal distribution of tumour intensity in cross-section for Case 1 –(a) and Case 2 –(b).

References

Bresch, D., Colin, T., Grenier, E., Ribba, B., Saut, O., 2010. Computational modeling of solid tumor growth: The avascular stage. SIAM J. Sci. Comput. 32, 2321–2344. http://dx.doi.org/10.1137/070708895.

Cai, Y., Wu, J., Li, Z., Long, Q., 2016. Mathematical modelling of a brain tumour initiation and early development: A coupled model of glioblastoma growth, pre-existing vessel co-option, angiogenesis and blood perfusion. PLoS One 11, e0150296. http://dx.doi.org/10.1371/journal.pone.0150296.

Chaplain, M., 1996. Avascular growth, angiogenesis and vascular growth in solid tumours: the mathematical modelling of the stages of tumour development. Math. Comput. Modelling 23, 47–87.

Cristini, V., Lowengrub, J., Nie, Q., 2003. Nonlinear simulation of tumor growth. J. Math. Biol. 46, 191–224. http://dx.doi.org/10.1007/s00285-002-0174-6.

Donatelli, D., Trivisa, K., 2015. On a nonlinear model for tumour growth with drug application. Nonlinearity 28, 1463. http://dx.doi.org/10.1088/0951-7715/28/5/1463.

Dyniewicz, B., Bajkowski, J.M., Bajer, C.I., 2023. Efficient strategy for space–time based finite element analysis of vibrating structures. Comput. Math. Appl. 148, 70–80. http://dx.doi.org/10.1016/j.camwa.2023.08.002.

Hahnfeldt, P., Panigrahy, D., Folkman, J., Hlatky, L., 1999. Tumor development under angiogenic signaling: a dynamical theory of tumor growth, treatment response, and postvascular dormancy. Cancer Res. 59, 4770–4775.

Hubbard, M.E., Byrne, H.M., 2013. Multiphase modelling of vascular tumour growth in two spatial dimensions. J. Theoret. Biol. 316, 70–89. http://dx.doi.org/10.1016/j.jtbi.2012.09.031.

Koomullil, R., Tehrani, B., Goliwas, K., Wang, Y., Ponnazhagan, S., Berry, J., Deshane, J., 2021. Computational simulation of exosome transport in tumor microenvironment. Front. Med. (Lausanne) 8, 643793. http://dx.doi.org/10.3389/fmed.2021.643793.

Lefebvre, G., Cornelis, F., Cumsille, P., Colin, T., Poignard, C., Saut, O., 2016. Spatial modelling of tumour drug resistance: The case of gist liver metastasis. Math. Med. Biol. http://dx.doi.org/10.1093/imammb/dqw002.

Lowengrub, J., Frieboes, H., Jin, F., Chuang, Y.L., Li, X., Macklin, P., Wise, S., Cristini, V., 2010. Nonlinear modelling of cancer: Bridging the gap between cells and tumours. Nonlinearity 23, R1–R91. http://dx.doi.org/10.1016/0895-7177(96)00019-2.

Lundgren, B., 1977. Observations of growth rate of breath carcinomas and its possible implications for lead time. Cancer 40, 1722–1725.

Mao, X., Zhou, M., Fan, C., Chen, B., Jin, F., 2019. Timescale of tumor volume of a young breast cancer patient with luminal B subtype. Medicine 98, e17659. http://dx.doi.org/10.1097/MD.0000000000017659.

Masannat, Y.A., Agrawal, A., Maraqa, L., Fuller, M., Down, S.K., Tang, S., Pang, D., Kontos, M., Romics, L., Heys, S.D., 2019. Multifocal and multicentric breast cancer, is it time to think again? Ann. R. Coll. Surg. Engl. 40, 62–66.

Watanabe, Y., Dahlman, E.L., Leder, K.Z., Hui, S.K., 2016. A mathematical model of tumor growth and its response to single irradiation. Theor. Biol. Med. Model. 13, http://dx.doi.org/10.1186/s12976-016-0032-7.

Weedon-Fekjaer, H., Lindqvist, B.H., Vatten, L.J., Aalen, O.O., Tretli, S., 2008. Breast cancer tumor growth estimated through mammography screening data. Breast Cancer Res 10, R41. http://dx.doi.org/10.1186/bcr2092.